Featured in Physics

Self-propulsion of a freely suspended swimmer by a swirling tail in a viscoelastic fluid

Jeremy P. Binagia [1,*] and Eric S. G. Shaqfeh [1,2,†]
[1]*Department of Chemical Engineering, Stanford University, Stanford, California 94305, USA*
[2]*Department of Mechanical Engineering, Stanford University, Stanford, California 94305, USA*

(Received 3 February 2021; accepted 9 April 2021; published 11 May 2021)

Microscopic organisms must frequently swim through complex biofluids, including bacterial biofilms and the mucus lining of the upper respiratory tract. Recently, there has been great interest in understanding how the non-Newtonian behavior of the fluids, in particular fluid elasticity, can enable methods of self-propulsion that otherwise would not work in a Newtonian fluid. We present such a swimmer that consists of two spheres of unequal size that rotate in opposite directions. The swimmer is force- and torque-free and placed in an elastic fluid. Using a combination of analytical theory and numerical simulations, we show that this model swimmer, which has zero propulsion in a Newtonian fluid under Stokes flow, swims in the direction of the larger of the two spheres in an elastic fluid. We show that the speed of swimming increases nearly linearly with the Deborah number De or primary normal stress coefficient Ψ_1, which is an appropriate measure of the elasticity of the fluid and for $\mathrm{De} \leqslant 1$ is also nearly linear in the concentration of polymer in the fluid. The dependence of the swim speed on the relative size of the two spheres is nonmonotonic, exhibiting a maximum at a size ratio of about 0.75. By analyzing the forces acting on the swimmer and the surrounding flow field, we find that propulsion is driven by thrust due to pressure applied along the swimmer. This thrust originates from flow advection driven by hoop stresses surrounding the faster-spinning smaller sphere. We compare our predictions to experimental measurements of swimming speeds for the bacterium *E. coli*, which swims via a rotating flagellar bundle and counterrotating body, and find that the speeds predicted by our analysis are remarkably close to the speed increase *E. coli* experiences in viscoelastic fluids. Finally, we conclude our work by showing how our analysis can be extended to different swimmer configurations and gaits, as long as the propulsion is driven by swirl alone.

DOI: 10.1103/PhysRevFluids.6.053301

I. INTRODUCTION

Recently, there has been a great deal of work examining the fundamental fluid mechanics of the motion of swimming microorganisms [1–3]. Of particular interest is their motility in complex fluids, since the biofluids in which these microorganisms are commonly immersed (e.g., biofilms [4,5] and mucus in the human body [6,7]) very often exhibit significant non-Newtonian behavior [8]. One active area of research is focused on developing and understanding propulsion mechanisms that otherwise would be ineffectual in a Newtonian fluid since, for example, translation via reciprocal motion is forbidden at zero Reynolds number [9]. Such microswimmers in non-Newtonian fluids could be used in biomedical applications such as targeted drug delivery [10,11] or could serve

*jbinagia@stanford.edu
†esgs@stanford.edu

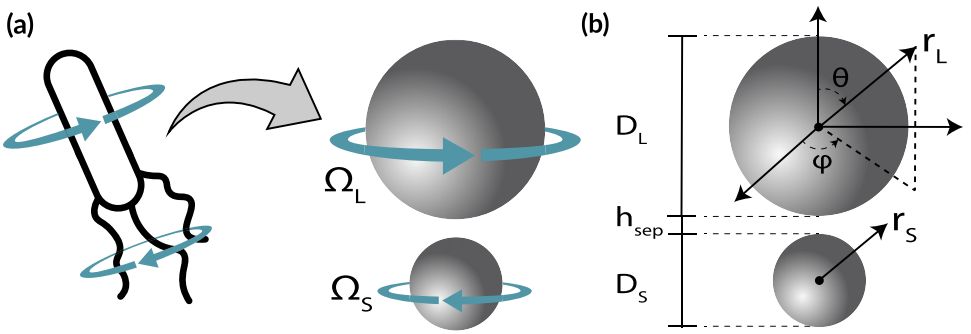

FIG. 1. (a) Depiction of a swimming *E. coli* cell (left) and the schematic of a coarse-grained model swimmer (right) that can be tuned to reproduce the azimuthal flow field created by the *E. coli* rotating flagellar bundle and counterrotating body. (b) Dimensions and coordinate system for the model two-sphere swimmer.

as a microrheometer for the fluid itself [12]. Some of these proposed swimming mechanisms include a synthetic microscallop [13], a sphere dimer rotated in a reciprocal motion by an external magnetic field [14], and a model swimmer consisting of two spheres that oscillate along their axis of symmetry [15]. While these swimmers achieve net translation by utilizing a reciprocal gait in an elastic fluid, propulsion can also be achieved by leveraging normal stress differences in viscoelastic fluids to break symmetry [16,17].

One example of propulsion in non-Newtonian fluids was examined by Pak *et al*. [12] and Puente-Velázquez *et al*. [18], who consider a body comprised of two rigid spheres that undergoes net translational motion along the axis of symmetry in a viscoelastic fluid when rotated by a net torque (e.g., provided by an external magnetic field). However, the propulsion examined by Pak *et al*. [12] does not apply to a torque-free swimming microorganism. We are inspired by Pak *et al*. [12] to develop a coarse-grained model swimmer that is force- and torque-free and can be realized experimentally. Moreover, such a swimmer can be used to study the effect of rheology on the motion of swimming microorganisms, particularly those whose gait induces a significant degree of swirling flow, e.g., the bacterium *E. coli* [19,20] [cf. Fig. 1(a)]. Our interest in this particular class of swimmers comes from recent work demonstrating the significance of rotational-translational coupling in predicting the kinematics of passive and active particles [21–23], i.e., that swirl aids propulsion in elastic fluids. Other studies [24–26] have also demonstrated the importance of swirling flow in viscoelastic fluids by considering helical swimmers, although it should be noted that in these cases the swimmer is not torque-free. The distinction from this prior work and the reason for this present effort is that the specific squirmer slip velocity containing swirl in [22,23] showed that swirl aided propulsion in viscoelastic fluids, but the swirl did not create propulsion alone. In contrast, as we will demonstrate, the microswimmer shown in Fig. 1 merely requires spinning two spheres in opposite directions connected by a fixed link to achieve propulsion of the freely suspended body.

II. GOVERNING EQUATIONS AND SOLUTION METHODOLOGY

We begin by noting the geometry and arrangement of our model microswimmer. The situation is illustrated in Fig. 1(b), where the two-sphere swimmer is oriented vertically along the z direction with the larger sphere placed above the smaller sphere. Here R_L and D_L denote the radius and diameter of the larger sphere, while R_S and D_S refer to the radius and diameter of the smaller sphere. The spheres counterrotate, and let us assume the larger sphere rotates counterclockwise (looking from above) with a rotation rate Ω_L, while the smaller sphere rotates clockwise with a rotation rate Ω_S. Note that Ω_L and Ω_S denote only the magnitude of the angular velocity, not the direction (i.e., they are always positive quantities). Finally, the gap between the two spheres is of size h_{sep} such that the distance between the centers of the two spheres is given by $h' = R_L + h_{\text{sep}} + R_S$.

For the fluid surrounding the microswimmer, the equations for conservation of momentum and mass written in dimensionless form are

$$\mathrm{Re}\left(\frac{\partial \mathbf{u}}{\partial t} + \mathbf{u}\cdot\nabla\mathbf{u}\right) = \nabla\cdot\boldsymbol{\sigma}, \quad \nabla\cdot\mathbf{u} = \mathbf{0}, \tag{1}$$

where $\mathbf{u}$ is the velocity of the fluid, t is time, and $\boldsymbol{\sigma}$ is the Cauchy stress. We have chosen to scale lengths by the radius of the larger sphere R_L, time by the inverse of the smaller sphere's rotation rate Ω_S^{-1}, velocities by the product $R_L\Omega_S$, and stresses by $\mu_0\Omega_S$, where μ_0 is the total zero-shear viscosity of the fluid. Note that we use Ω_S rather than Ω_L in our scaling since in our application the former is considered "prescribed" as the rotation rate of the swimmer's tail, while the latter is determined by the fact that the total torque on the swimmer vanishes. With this choice of characteristic scales, the Reynolds number Re is given by $\mathrm{Re} = \rho R_L^2\Omega_S/\mu_0$, where ρ is the density of the fluid. Owing to their small size and the viscous environments in which they are commonly found, microorganisms swim at virtually zero Reynolds number [9]. For this reason, in both our analytical theory and numerical simulations we assume $\mathrm{Re} = 0$.

We further assume that the fluid in which the microswimmer is immersed is viscoelastic; thus the total stress $\boldsymbol{\sigma}$ is given as the sum of a Newtonian and polymeric contribution

$$\boldsymbol{\sigma} = -p\mathbf{I} + \beta(\nabla\mathbf{u} + \nabla\mathbf{u}^T) + \boldsymbol{\tau}^p, \tag{2}$$

where p is the pressure, $\boldsymbol{\tau}^p$ is the extra stress from the polymer molecules in the fluid, and $\beta = \mu_s/(\mu_s+\mu_p) = \mu_s/\mu_0$ is the viscosity ratio for a fluid with solvent viscosity μ_s and polymer viscosity μ_p. To describe the extra polymer stress $\boldsymbol{\tau}^p$, we use the Oldroyd-B constitutive equation, which models the polymer molecules as Hookean dumbbells [27]:

$$\boldsymbol{\tau}^p = \frac{1-\beta}{\mathrm{De}}(\mathbf{c}-\mathbf{I}), \tag{3}$$

$$\mathrm{De}\,\overset{\triangledown}{\mathbf{c}} + (\mathbf{c}-\mathbf{I}) = \mathbf{0}. \tag{4}$$

In the above set of equations, $\mathbf{c}$ is the conformation tensor, $\overset{\triangledown}{\mathbf{c}} = \partial\mathbf{c}/\partial t + \mathbf{u}\cdot\nabla\mathbf{c} - \nabla\mathbf{u}^T\cdot\mathbf{c} - \mathbf{c}\cdot\nabla\mathbf{u}$ is the upper-convected derivative, and $\mathrm{De} = \lambda\Omega_S$ is the Deborah number, which measures the degree of elasticity of a viscoelastic fluid having a relaxation time λ.

These governing equations are supplemented by an appropriate set of boundary conditions and constraints applied to the swimming motion. Applying the no-slip boundary condition at the surface of the swimmer gives the velocity at the surface of the smaller sphere as $\mathbf{u}_S = \mathbf{U} + \boldsymbol{\Omega}_S\times\mathbf{r}_S$ and that at the surface of the larger sphere as $\mathbf{u}_L = \mathbf{U} + \boldsymbol{\Omega}_L\times\mathbf{r}_L$, where $\mathbf{U}$ is the velocity of the swimmer and $\mathbf{r}_S$ and $\mathbf{r}_L$ are position vectors originating from the center of the smaller and the larger sphere, respectively. Finally, upon applying conservation of linear and angular momentum to the swimming body in the limit of $\mathrm{Re} = 0$, one finds that the net force and torque on the microswimmer must vanish [28],

$$\mathbf{F} = \int_S \boldsymbol{\sigma}\cdot\mathbf{n}\,dS = \mathbf{0}, \tag{5}$$

$$\mathbf{L} = \int_S \mathbf{x}\times(\boldsymbol{\sigma}\cdot\mathbf{n})dS = \mathbf{0}, \tag{6}$$

in which S denotes the surface of the swimmer, $\mathbf{x}$ is the position vector for a coordinate system placed at the center of the gap between the two spheres, and $\mathbf{n}$ is the outward surface unit normal vector. Finally, the fluid far from the swimmer is stagnant, so $\mathbf{u}(|\mathbf{x}|\to\infty) = 0$.

In what follows we will use a combination of analytical theory and numerical simulations to determine the swimming speed of this model microswimmer subject to the above set of governing equations and boundary conditions. With respect to the former, our derivation is a generalization of that done in [18] and Sec. V of [12], but now the rotation rates of the two spheres Ω_S and Ω_L

are not necessarily equal since they are determined from the torque-free condition. We begin by considering the leading-order radial disturbance flow at small De for each sphere in isolation [29],

$$u_r^S(\theta, r_S) = r^*(1-\beta)\mathrm{De}\left[\frac{r^{*2}}{2r_S^2} - \frac{3r^{*4}}{2r_S^4} + \frac{r^{*5}}{r_S^5}\right](3\cos^2\theta - 1), \tag{7}$$

$$u_r^L(\theta, r_L) = \frac{(1-\beta)\mathrm{De}}{(\Omega^*)^2}\left[\frac{1}{2r_L^2} - \frac{3}{2r_L^4} + \frac{1}{r_L^5}\right](3\cos^2\theta - 1), \tag{8}$$

where $r_L = |\mathbf{r}_L|$, $r_S = |\mathbf{r}_S|$, and θ is the polar angle in the spherical coordinate system, as shown in Fig. 1(b). Additionally, two new dimensionless groups emerge: $\Omega^* = \Omega_S/\Omega_L$ is the ratio of the rotation rates of the two spheres and $r^* = R_S/R_L$ is the ratio of their radii. Finally, with r^* defined, we can write the distance between the centers of the spheres in dimensionless form as $h = 1 + h^* + r^*$, where $h* = h_{\mathrm{sep}}/R_L$. In the scenario where the two spheres are touching, $h^* = 0$ and $h = 1 + r^*$.

Owing to the axisymmetry of the problem, the x and y components of the net force $\mathbf{F}$ acting on the swimmer are trivially zero. This leaves us with the component acting in the z direction, F_z, which consists of drag from the steady translation of the swimmer as well as contributions from the hydrodynamic interactions between the two spheres. The sum of the latter two contributions is the propulsive contribution to the net force, i.e., $F_z = F^{\mathrm{drag}} + F^{\mathrm{prop}}$. We explicitly write this contribution as the sum of the force acting on the smaller sphere due to the flow field of the larger sphere and the force acting on the larger sphere due to the flow field of the smaller sphere. These are given approximately by Faxén's law [30], viz.,

$$F_z^{\mathrm{prop}} = 6\pi\left(1 + \frac{1}{6}\nabla^2\right)u_r^S(\theta = 0, r_S = h) - 6\pi r^*\left(1 + \frac{r^{*2}}{6}\nabla^2\right)u_r^L(\theta = \pi, r_L = h). \tag{9}$$

Note that in the above, as distinct from Sec. V of [12] and from [18], we have included the Laplacian term in Faxén's law since we find that it significantly improves the accuracy of the final result. It should be mentioned here that a more accurate prediction for the propulsive force and hence the swimming speed could likely be obtained by performing a formal perturbation expansion in the limit of small De, as was done in [12]. Satisfied with the agreement between theory and numerics shown in Sec. III, we forego this more detailed calculation in the interest of providing a final result that through its conciseness can yield greater physical intuition and more readily be employed to make predictions for a range of geometries and conditions.

We can estimate the speed of the microswimmer by noting that this propulsive force is equal and opposite to the viscous drag experienced by the swimmer, i.e., $F_z = F_z^{\mathrm{drag}} + F_z^{\mathrm{prop}} = 0$. As a simple approximation, we can estimate this drag using the hydrodynamic resistance for a Newtonian fluid, i.e., $F_z^{\mathrm{drag}} = -6\pi(1 + r^*)U_z$, so that the velocity (specifically the z component U_z) is given by

$$U_z = \frac{F_z^{\mathrm{prop}}}{6\pi(1 + r^*)}. \tag{10}$$

For the sake of presentation, we will split the contribution to U_z originating from the two terms that involve the Laplacian in Eq. (9) as $U_z^{(HO)}$. The velocity of the swimmer can then be written explicitly as

$$U_z = U_z^0 + U_z^{(HO)} = \frac{u_r^S - r^* u_r^L}{1 + r^*} + \frac{1}{6}\frac{\nabla^2 u_r^S - r^{*3}\nabla^2 u_r^L}{1 + r^*}. \tag{11}$$

We can express U_z in terms of the dimensionless groups r^*, h^*, De, β, and Ω^* by plugging in the velocity fields given in Eqs. (7) and (8) into Eq. (11) and we obtain

$$U_z^0 = \mathrm{De}(1-\beta)\frac{(1+h^*)^2 r^{*3}(1 + h^* + 3r^*)\Omega^{*2} - r^*(h^* + r^*)^2(3 + h^* + r^*)}{(1 + r^*)(1 + h^* + r^*)^5\Omega^{*2}} \tag{12}$$

and

$$U_z^{(HO)} = \mathrm{De}(1-\beta)r^{*3}\left(\frac{Q}{3(1+r^*)(1+h^*+r^*)^7\Omega^{*2}}\right), \tag{13}$$

where Q, the factor in the numerator of U_z^{HO}, is

$$\begin{aligned} Q(r^*, h^*, \Omega^*) = &-3 + 15h^* + 6h^{*2} + 2h^{*3} + 15r^* + 12h^*r^* + 6h^{*2}r^* + 6r^{*2} + 6h^*r^{*2} \\ &+ 2r^{*3} - [2(1+h^*)^3 + 6(1+h^*)^2r^* + 15(1+h^*)r^{*2} - 3r^{*3}]\Omega^{*2}. \end{aligned} \tag{14}$$

Note that, alternatively, since for the Oldroyd-B fluid the relaxation time is directly related to the primary normal stress coefficient Ψ_1 via the expression

$$\lambda = \frac{\Psi_1}{2\mu_p}, \tag{15}$$

we have expressed the propulsion velocity as linear in the primary normal stress coefficient and therefore a direct measure of the fluid elasticity via rheometry.

With this result in hand, we first consider specific subcases of the overall parameter space. For example, if we consider the situation where the two spheres are touching ($h^* = 0$) and are rotating together as a rigid body ($\Omega^* = 1$) and we neglect the higher-order terms in the propulsive force (achieved in effect by setting $U_z^{(HO)} = 0$), then we in fact recover the result derived from the use of Faxén's law in Sec. V of [12]:

$$U_z = \mathrm{De}(1-\beta)\frac{2(r^*-1)r^{*3}}{(1+r^*)^6}. \tag{16}$$

As stated above, we are interested in using this model swimmer to understand the effect of swirling flow on microorganism motility in complex biofluids. For a freely suspended swimmer, we must ensure that the two-sphere swimmer is torque-free, as is the case for all freely suspended microswimmers. This is achieved in our model by allowing the two spheres to rotate in opposite directions such that the net torque vanishes, regardless of the chosen size ratio r^*. Noting that the (dimensional) torque on a sphere rotating at $\mathrm{Re} = 0$ in a Newtonian fluid is equal in magnitude to $8\pi\mu_0\Omega R^3$, we see that the torques on the two spheres sum to zero when $\Omega^* = (1/r^*)^3$. Assuming the two spheres are touching ($h^* = 0$), we can then obtain a simplified result for the velocity:

$$U_z = \mathrm{De}(1-\beta)r^{*3}\frac{(1-r^*)(1+10r^*+16r^{*2}+28r^{*3}+28r^{*4}+28r^{*5}+16r^{*6}+10r^{*7}+r^{*8})}{3(1+r^*)^8}. \tag{17}$$

Note that the assumption in taking this limit ($h^* = 0$) is that the propulsion speed is regular as $h^* \to 0$. We demonstrate via lubrication theory in the Appendix that while the flow demonstrates a pressure singularity in this limit, the propulsion speed is bounded as $h^* \to 0$, which is demonstrated in Fig. 4 below as well. One can easily verify that the numerator of the fraction in Eq. (17) is positive for $0 \leqslant r^* \leqslant 1$, indicating $U_z > 0$ for all values of De and β; in other words, our model predicts that a torque-free two-sphere swimmer always swims in the direction of the larger sphere for any size ratio and specific Oldroyd-B fluid rheology. For the remainder of this study, we will use our theory [i.e., (12), (13), and (17)] and complementary numerical simulations to understand this result.

For the numerical calculations, we perform three-dimensional simulations of the governing equations and boundary conditions using a third-order-accurate finite-volume flow solver developed at Stanford's Center for Turbulence Research [31]. As detailed in a number of previous studies, this code has been thoroughly tested for accuracy and robustness for a wide range of problems, including viscoelastic flows [32–34], deformable particles [35], and active swimmers [36]. Specifically for this problem, the numerical solution closely follows that described in our previous work [22]; namely, we consider the comoving frame of reference such that we may use a body-fitted mesh, the evolution

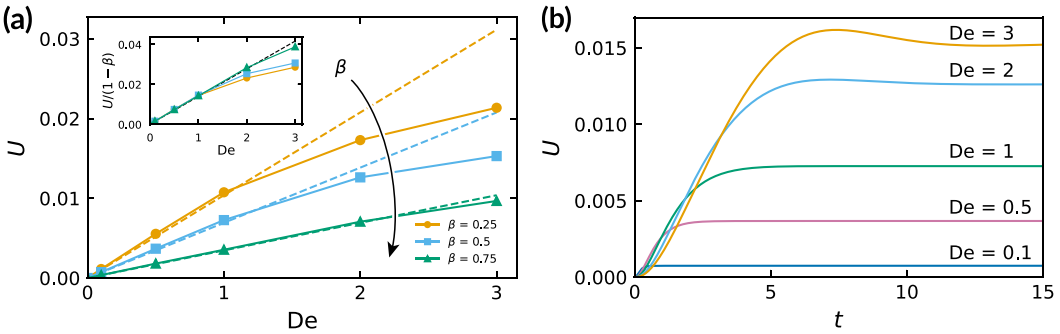

FIG. 2. (a) Swimming speed U as a function of the Deborah number De and the viscosity ratio β for $h^* = 0.05$ and $r^* = 0.5$. Markers connected by solid lines denote simulation data, while the dashed lines denote the low-De theory, i.e., Eqs. (12) and (13). As indicated by the black arrow, as one moves down the set of curves, the value of β increases from 0.25 to 0.75, i.e., an increasing contribution from the Newtonian solvent. The theory and simulations show that the speed of the two-sphere swimmer increases with increasing fluid elasticity (De) and increasing polymer concentration (decreasing β). The inset shows the same set of data but with the speed U now normalized by $1 - \beta$ to show that all data collapses onto a single curve for low De, as predicted by the theory. (b) Swimming speed U as a function of time for $h^* = 0.05$, $r^* = 0.5$, and $\beta = 0.5$.

equation for the conformation tensor [Eq. (4)] is solved using the log-conformation method [37,38], and for boundary conditions for the conformation tensor we set $\mathbf{c} = \mathbf{I}$ at the entrance to the domain and utilize a convective outlet boundary condition at the exit. We use a cylindrical computational domain of length and diameter $20R_L$, whose axis of revolution is aligned with the z direction and in which the two-sphere swimmer shown in Fig. 1 is placed at the center. To resolve the stress boundary layers present near the swimmer, we use an unstructured tetrahedral mesh with increasing resolution towards the center of the domain. To determine the kinematics of the two-sphere swimmer, we advance Eq. (1) forward in time, solving for U_z and Ω_L at each time step such that $F_z = 0$ and $L_z = 0$ by using a quasi-Newton method, specifically Broyden's method [39]. We prescribe a dimensionless rotation rate of the smaller sphere equal to unity for all t while the initial condition for our simulations is that of a quiescent fluid with $\mathbf{c} = \mathbf{I}$; this results in $U_z(t = 0) = 0$ and $\Omega_L(t = 0)$ being determined from the torque balance at the start of the simulation.

III. RESULTS, DISCUSSION, AND MORE GENERAL SWIMMERS

A. Speed and mechanism of propulsion for the two-sphere swimmer

With our theory and numerical simulations described above, we proceed to discuss our results, starting with the dependence of the swimming speed on the rheology of the surrounding fluid when the swimmer has achieved steady state. The results are shown in Fig. 2(a), where the swimming speed $U = |U_z|$ is plotted as a function of the Deborah number for the case of $\beta = 0.5$ and $r^* = 0.5$. Note that in Fig. 2 we assume $h^* = 0.05$; choosing a small but nonzero value of h^* in this way allows us to consider the case where the two vortical flows induced by the spheres are interacting with one another (as they likely are for real microorganisms like *E. coli*), but the gap is still large enough such that the stress within it can be resolved numerically (cf. Fig. 6). From this plot we see that both theory (dashed lines) and simulations (closed symbols) indicate an increase in swimming speed with fluid elasticity (increasing De) and increasing polymer concentration (decreasing β). The theory agrees remarkably well with the simulations, with the agreement increasing as the fraction of the fluid that is Newtonian solvent increases. Thus, for small values of β, the theoretical and numerical predictions depart from one another for De > 1, with the theory overpredicting the swimming speed observed in simulations. The inset shows that for small De, the swimming speed increases linearly with respect to $(1 - \beta)$De, as is predicted by the theory.

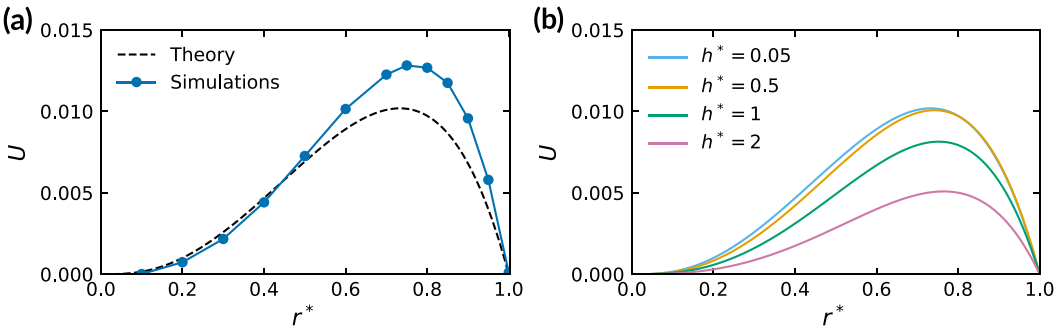

FIG. 3. (a) Swimming speed U as a function of the size ratio r^* for $h^* = 0.05$, De $= 1$, and $\beta = 0.5$. Both theory and simulations predict a nonmonotonic dependence of U on r^*, with U vanishing in the case of $r^* = 0$ and 1, while reaching a maximum at $r^* \approx 0.75$. (b) Theoretical prediction for the swimming speed U as a function of the size ratio r^* for De $= 1$, $\beta = 0.5$, and a range of values of h^*. As h^* is increased, U decreases in magnitude for all r^*. However, the functional dependence of U with respect to r^* is not strongly affected by the value of h^*.

In Fig. 2(b) the swimming speed U is plotted as a function of time for $h^* = 0.05$, $r^* = 0.5$, $\beta = 0.5$, and for the range of De shown in Fig. 2(a). From this figure we can see how the two-sphere swimmer reaches a steady-state speed starting from rest. We see that the time to reach steady state increases with increasing De. For small to moderate values of De, the speed increases monotonically until the steady-state speed is reached. For large values of De (e.g., De $= 3$), however, there is an overshoot in the swimming speed prior to reaching the steady-state value. As we see in Fig. 2(b), it takes between 0.1 and 0.8 rotations of the small-sphere tail to reach steady state for De $\leqslant 1$.

In Fig. 3(a) the swimming speed U is plotted as a function of the relative size of the two spheres r^* for the case of $\beta = 0.5$, De $= 1$, and $h^* = 0.05$. From this plot we see that the speed of the two-sphere swimmer exhibits a nonmonotonic dependence on r^*, with U vanishing for either $r^* = 0$ or $r^* = 1$. Both theory and simulations predict that the speed is approximately maximized at a size ratio of about 0.75, with the theory underpredicting the quantitative value of the maximum speed. We believe the disagreement for this range of size ratios is a manifestation of the far-field assumption inherent in applying Faxén's law. That is, Faxén's law prescribes the force on a particle as that due to the external flow (from another particle) applied at its center and the Laplacian of that flow; this is valid when the particles are well separated but is inaccurate in the near field. In other words, as the sizes of the two spheres become comparable, higher-order hydrodynamic reflections become significant and need to be taken into account for a quantitative theory. Neglecting these interactions is fine for smaller values of r^* since as r^* decreases, the larger sphere is increasingly in the far field of the smaller sphere.

To understand how this picture changes as the gap size is altered, in Fig. 3(b) we have plotted the theoretical prediction of the swimming speed U as a function of r^* for a range of values of h^*. Interestingly, up to a gap size of $h^* = 0.5$, there appears to be little effect with respect to increasing h^*. Past $h^* = 0.5$, an increase in h^* leads to a decrease in swimming speed for all values of r^* and a very slight increase in the location of the optimal size ratio. To explore the effect of the gap size further, in Fig. 4 we have plotted the swimming speed U normalized by the factor De$(1 - \beta)$ as a function of h^* for both theory and simulations for the case of $r^* = 0.75$. We divide U by De$(1 - \beta)$ in this case to isolate the effect of geometry; e.g., as shown in Eqs. (12) and (13), $U/\text{De}(1 - \beta)$ depends solely on the size ratio r^* and gap size h^* [recall we have taken $\Omega^* = (1/r^*)^3$]. From this figure we see that the theory predicts a very slight increase in swimming speed with increasing gap size before exhibiting a monotonic decay. The numerical results, in contrast, suggest that the swimming speed only decreases with increasing gap size. The agreement between theory and simulations becomes better with increasing gap size, as expected given the

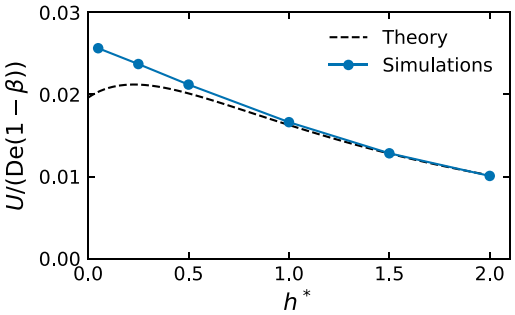

FIG. 4. Normalized swimming speed $U/\mathrm{De}(1-\beta)$ as a function of the gap size h^* for a size ratio of $r^* = 0.75$. The numerical simulations were conducted at $\mathrm{De} = 1$ and $\beta = 0.5$. While the theory predicts a slight increase in the swimming speed before a monotonic decrease with increasing gap size, the simulation results predict a purely decreasing function of gap size. As expected, the two predict the same result for large values of h^* since the theory becomes more accurate as the separation increases.

far-field approximations made in our derivation. Taking this into account, i.e., that we expect the theory to become less accurate for very small gap sizes, and considering that the simulations are valid for any geometry, we believe that the true trend with respect to the gap size is a monotonic decrease in speed.

We now turn to an examination of the forces acting on the microswimmer and the surrounding flow field in an effort to understand the origin of the self-propulsion observed in Figs. 2 and 3. We split the contributions to the net hydrodynamic force in accordance with Eq. (2) as those due to pressure, viscous stress, and polymeric stress (written using indicial notation assuming cylindrical coordinates): $F_z = \int_S \sigma_{zj} n_j dS = F_z^{\mathrm{pres}} + F_z^{\mathrm{visc}} + F_z^{\mathrm{poly}} = 0$, where $F_z^{\mathrm{pres}} = -\int_S p n_z dS$, $F_z^{\mathrm{visc}} = \beta \int_S (\nabla_z u_j + \nabla_j u_z) n_j dS$, and $F_z^{\mathrm{poly}} = \int_S \tau_{zj}^p n_j dS$. These contributions are plotted as a function of De in Fig. 5(b). We see from Fig. 5(a), where these contributions are further divided into those acting on the large and the small sphere, respectively, that the contribution due to pressure dominates the force on both the larger (indicated with the dash-dotted line) and the smaller (indicated with a

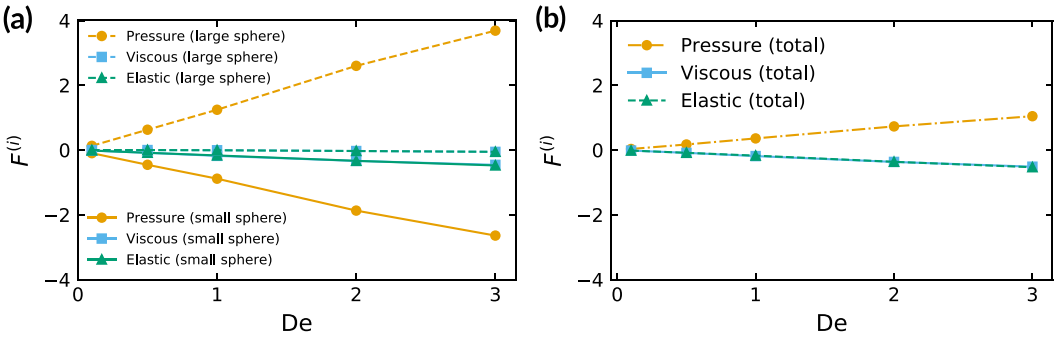

FIG. 5. Contributions to the net force acting on the swimmer as a function of De for $h^* = 0.05$, $r^* = 0.5$, and $\beta = 0.5$. (a) Total integrated force contributions acting on each sphere. Solid lines denote forces on the smaller sphere, while dash-dotted lines denote force on the larger sphere. The plot indicates that pressure acting on the larger sphere creates a positive (i.e., propulsive) contribution to the net hydrodynamic force, while contributions from pressure, viscous, and elastic stresses acting on the smaller sphere are negative and thus oppose the swimming motion. (b) Total integrated force contributions acting over the entire swimmer (i.e., summing individual forces acting on the large and the small sphere). This plot indicates that the net effect of pressure is propulsive, while those of viscous and elastic stresses are resistive.

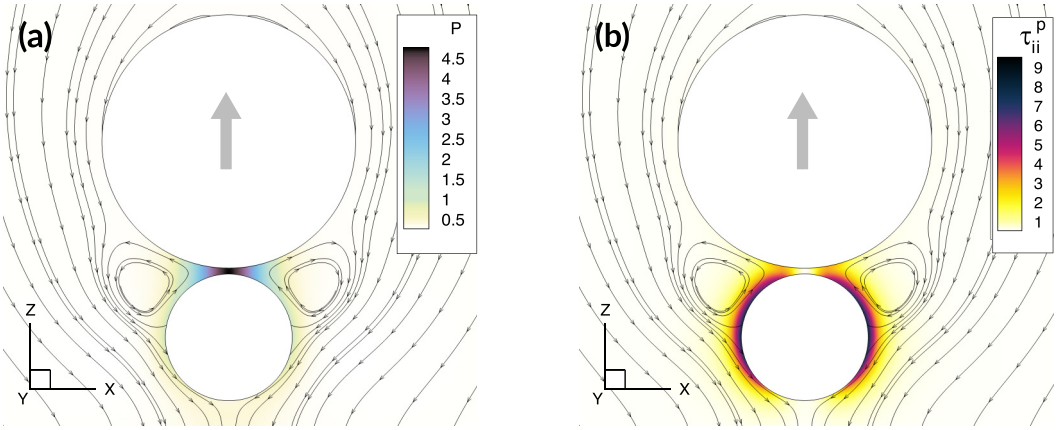

FIG. 6. Contour plots in the x-z plane at $y = 0$ of (a) the pressure and (b) the polymer stress energy τ_{ii}^{p} for the simulation at De $= 1$, $\beta = 0.5$, $h^* = 0.05$, and $r^* = 0.5$. Streamlines indicate the direction of the radial flow field in the comoving frame of reference; the gray arrow in each panel indicates the swimming direction in the laboratory frame. Given the results shown in Fig. 5, propulsion appears to created by a buildup of pressure towards the rear of the swimmer that originates from flow pulled inward from the faster-spinning smaller sphere. In (b) we see the development of hoop stresses from the rotation of the smaller sphere that otherwise act to impede motion according to Fig. 5.

solid line) sphere. The former is the seemingly only positive contribution to the net force on the swimmer, indicating that it is pressure on the larger sphere that provides the dominant thrust for the microswimmer's motion. In contrast, all of the contributions related to the smaller sphere are negative and thus oppose the motion of the swimmer. This suggests that the drag on the overall body is concentrated at the back of the swimmer and thus on the smaller sphere.

To understand this mechanism of self-propulsion in more detail, we now examine the surrounding flow field to see exactly where tractions are being exerted on the swimmer. From Fig. 6(a) we see that there is a significant pressure in the small gap between the two rotating spheres. If we examine the streamlines of the radial flow field (presented in the comoving frame) while recalling that the swimmer translates in the direction of the larger sphere (as indicated by the gray arrow), we see that fluid is readily advected by the fast-spinning smaller sphere, thereby creating a high-pressure region in the thin gap and along its sides. Hence, in analogy with *E. coli* [cf. Fig. 1(a)], it appears that the fast-spinning tail of our model swimmer pulls fluid inward so as to create an overall thrust due to pressure. Interestingly enough, the net effect of the pressure specifically in the thin-gap region is zero; i.e., the pressure tractions exerted on the larger and the smaller sphere in this region cancel each other. We show this below by applying lubrication theory to the thin-gap region. While we refer the reader to the Appendix for the full derivation, the key result is that the pressure in the gap is given by

$$p = \mathrm{De}(1-\beta)\frac{(\Omega^*+1)^2}{B(h^*+Br^2)}, \tag{18}$$

where $B = \frac{1}{2}(r^{*-1}+1)$ and r is the radial coordinate in cylindrical coordinates (made dimensionless by R_L). A comparison of the pressure as predicted by this equation to that from our numerical simulations is shown in Fig. 7. This demonstrates that in the limit of $h^* \to 0$, there is a pressure singularity. However, if we integrate this function over the surface of the large and the small sphere in the thin-gap region, we find that the result is zero, i.e., the individual pressure forces exerted on each sphere are equal and opposite. This suggests that the net pressure thrust seen in Fig. 5(b) is not coming from the high pressure in the thin gap, but rather from the pressure observed at the back of

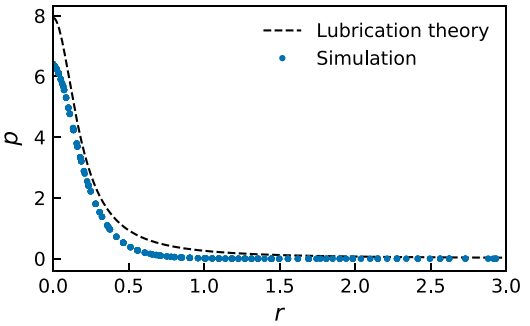

FIG. 7. Comparison of the pressure p predicted by lubrication theory [i.e., Eq. (18)] to that from our numerical simulation as a function of the radial coordinate r in cylindrical coordinates for the case of $r^* = 0.5$, $h^* = 0.05$, $\beta = 0.5$, and $\mathrm{De} = 1$.

the smaller sphere and swimmer as a whole as seen in Fig. 6(a). This makes sense in light of the results varying the gap size [i.e., Fig. 3(b) and Fig. 4]; that is, if the thrust had been primarily due to the high pressure in the thin gap, then we would expect to see a strong dependence of the swimming speed on the size of the gap. Finally, if we plot the polymer stress energy τ_{ii}^p, i.e., the trace of the polymer stress tensor, as done in Fig. 6(b), we observe the development of hoop stresses created by the fast-rotating smaller sphere. This likely corresponds to the negative elastic contribution to the net force seen in Fig. 5(b), suggesting that the elasticity of the fluid directly only hinders motion, but indirectly can provide thrust through a modification of the pressure field (an effect seen previously in several different studies [21,23]).

A natural question to ask is how the results presented above relate to a real microorganism. We can perform an approximate calculation to determine the appropriate values for r^*, β, and De for a bacterium like *E. coli* and compare the swimming speed of *E. coli* in a viscoelastic fluid to that predicted by our theory and simulations. For this, we reference the work of Patteson *et al.* [40], where they measure a swimming speed of about 11.2 μm/s in a 225 ppm carboxymethyl cellulose (CMC) solution. To put this speed in dimensionless terms, we scale it by $R_L\Omega_S$, where for the value of R_L we consider the radius of the *E. coli* body and for Ω_S we use the angular frequency of the flagellar bundle. The former is about 0.4 μm [19], while the latter was measured by Patteson *et al.* [40] to be 56 Hz (i.e., approximately equal to 352 rad/s) in the CMC solution. This yields a dimensionless speed of $11.2/(0.4 \times 352) \approx 0.08$. For the value of R_S and thus r^*, we use the radius of one of the *E. coli* helical flagella, which is about 0.4 μm [19] such that $r^* \approx 0.5$. Finally, to compute appropriate values for β and De, we note the measured value of $\lambda = 9.5 \times 10^{-3}$ s in the work of Patteson *et al.* [40] and then fit their data for the shear viscosity as a function of shear rate to a polymer constitutive equation that exhibits shear thinning, specifically the Giesekus equation [41]. From this fit we estimate that $\beta \approx 0.1$, and since $\mathrm{De} = \lambda\Omega_S$, $\mathrm{De} \approx 9.5 \times 10^{-3} \times 352 = 3.3$. Our nearest simulation to $r^* = 0.5$, $\beta = 0.1$, and $\mathrm{De} = 3.3$ is at $r^* = 0.5$, $\beta = 0.25$, and $\mathrm{De} = 3$, where we predict a speed of about 0.021. If we consider the dependence on β to be linear in $1 - \beta$ as predicted by the theory, then we expect our simulations to yield a speed of $0.021 \times (1 - 0.1)/(1 - 0.25) \approx 0.025$ at this smaller value of β. This value is thus about 31% of the experimentally measured swimming speed of *E. coli*, suggesting that the propulsion mechanism as described above from swirling flow could account for up to about one-third of the *E. coli* motility in viscoelastic fluids. If we assume that the remaining 69% of the swimming speed is a product of the viscous propulsion generated from rotating a helix at zero Reynolds number [20], then we expect the Newtonian speed of *E. coli* to be about two-thirds that in the elastic fluid. Patteson *et al.* [40] measured a Newtonian swimming speed of 8.3 μm/s, which is 74% that in the 225 ppm solution and is remarkably close to the value of 69% predicted by our simple estimation.

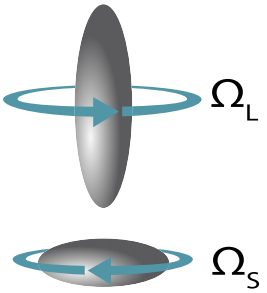

FIG. 8. Illustration of one particular example of an axisymmetric swimmer consisting of two counterrotating bodies of revolution.

B. Generalization to arbitrary bodies of revolution

While the results above were presented in the context of the two-sphere swimmer, similar arguments in the derivation of the theory can be made for arbitrary bodies of revolution (e.g., ellipsoids and cones). For example, consider a swimmer consisting of two axisymmetric shapes of different sizes that are rotating in opposite directions about the axis of symmetry (cf. Fig. 8). We define length scales for the smaller and the larger of these two bodies through the torque they exert on the surrounding fluid at $\mathrm{Re} = 0$, i.e.,

$$L_z^{\prime,S} = -8\pi\mu_0 l_S^3 \Omega_S, \tag{19}$$

$$L_z^{\prime,L} = 8\pi\mu_0 l_L^3 \Omega_L, \tag{20}$$

where $(\,)'$ denotes a dimensional quantity. The requirement of no torque on the combined body thus gives $\Omega^* = \Omega_S/\Omega_L = l_L^3/l_S^3 = 1/r^{*3}$. In the far field from the representation theorem in Newtonian Stokes flow, these rotating objects produce a rotlet disturbance flow such that their respective flow fields in isolation are given by [30]

$$u_\phi^{\prime,S} = -\frac{l_S^3 \Omega_S \sin\theta}{r_S^2}, \tag{21}$$

$$u_\phi^{\prime,L} = \frac{l_L^3 \Omega_L \sin\theta}{r_L^2}. \tag{22}$$

Note that this is exactly the flow created by a rotating sphere in Stokes flow, with the length scales l_S and l_L taking the place of the sphere's radius. It follows that to first order in De, the far-field radial velocities are the most slowly decaying terms in Eqs. (7) and (8), viz.,

$$u_r^{\prime,S}(\theta, r_S') = l_S^3 \Omega_S^2 \lambda \frac{3\cos^2\theta - 1}{2r_S'^2}, \tag{23}$$

$$u_r^{\prime,L}(\theta, r_L') = l_L^3 \Omega_L^2 \lambda \frac{3\cos^2\theta - 1}{2r_L'^2}. \tag{24}$$

Assuming these far-field velocities are the largest contribution, we can write the propulsive force as the difference between the force exerted on the larger body by the smaller body and vice versa,

$$F_z^{\prime,\mathrm{prop}} = D_L \mu_0 l_L u_r^{\prime,S,}(\theta = 0, r_S' = h') - D_S \mu_0 l_S u_r^{\prime,L}(\theta = \pi, r_L' = h'), \tag{25}$$

$$F_z^{\prime,\mathrm{prop}} = D_L \mu_0 l_L \left[\frac{l_S^3 \Omega_S^2 \lambda}{h'^2}\right] - D_S \mu_0 l_S \left[\frac{l_L^3 \Omega_L^2 \lambda}{h'^2}\right], \tag{26}$$

where we have used an approximation to Faxén's law for bodies of revolution [30]. Note that h' is the dimensional distance between the center of mass of each body. Thus we might anticipate a net propulsive force as before, but now accounting for the particular shape of the two halves of the swimmer via drag coefficients D_S and D_L. By factoring this expression, we can determine under what conditions we expect propulsion in the positive z direction:

$$F_z'^{,\mathrm{prop}} = \frac{D_L \mu_0 l_L l_S^3 \Omega_S^2 \lambda}{h'^2}\left(1 - \frac{D_S}{D_L}\frac{l_S}{l_L}\frac{\Omega_L^2 l_L^3}{\Omega_S^2 l_S^3}\right). \tag{27}$$

For self-propulsion in the positive z direction, we need $F_z'^{,\mathrm{prop}} > 0$, meaning that the expression in parentheses in Eq. (27) must be positive. Note though that for the swimmer to be torque-free, $\Omega_L/\Omega_S = l_S^3/l_L^3$. Thus, for $F_z'^{,\mathrm{prop}}$ to be positive, indicating propulsion towards the larger body, it must be the case that

$$1 - \frac{D_S}{D_L}\frac{l_S}{l_L}\frac{\Omega_L^2 l_L^3}{\Omega_S^2 l_S^3} > 0, \tag{28}$$

$$\frac{D_S}{D_L}\frac{l_S}{l_L}\frac{\Omega_L^2 l_L^3}{\Omega_S^2 l_S^3} < 1, \tag{29}$$

$$\frac{D_S}{D_L}\frac{l_S^4}{l_L^4} < 1, \tag{30}$$

i.e., there is net propulsion if $D_L l_L^4/D_S l_S^4 > 1$. Thus, using the effective lengths and the drag coefficients of the two-body swimmer, the criterion above can be used to predict propulsion by swirl in viscoelastic fluids.

The drag resulting from translation of the swimmer in the z direction is given by $-\mu_0(D_L l_L + D_S l_S)U_z'$; thus, using only the far-field flow as an approximation and balancing the propulsive and drag force yields, for U_z',

$$U_z' = \frac{F_z'^{,\mathrm{prop}}}{\mu_0(D_L l_L + D_S l_S)}, \tag{31}$$

$$U_z' = \frac{D_L l_L l_S^3 \Omega_S^2 \lambda}{h'^2(D_L l_L + D_S l_S)}\left(1 - \frac{D_S}{D_L}\frac{l_S^4}{l_L^4}\right), \tag{32}$$

or in dimensionless terms

$$U_z = \frac{D_L r^{*3}\mathrm{De}}{h^2(D_L + r^* D_S)}\left(1 - \frac{D_S}{D_L} r^{*4}\right). \tag{33}$$

To illustrate the utility of our criteria for propulsion in the direction of the larger body, $D_L l_L^4/D_S l_S^4 > 1$, we consider a specific axisymmetric swimmer consisting of a spherical head and prolate spheroidal tail oriented in the vertical z direction [cf. Fig. 9(a)]. The diameter of the spherical head is D_L, while the dimensions of the spheroidal tail are given by its polar radius a and equatorial radius c. To study how the relative sizes of the head and tail affect the direction of propulsion, we vary the polar radius of the tail while maintaining $c/R_L = 0.75$. We consider five such swimmers with tail aspect ratios c/a equal to 1, 2, 2.75, 3.6, and 4. For each swimmer, we measure its velocity in the z direction and compute the ratio $D_L l_L^4/D_S l_S^4$ for its specific geometry using formulas provided in [30] to compute translational and rotational resistance coefficients for prolate spheroids.

The results are shown in Fig. 9(b), where the swimming speed is plotted as a function of the ratio $D_L l_L^4/D_S l_S^4$ in the case of $\mathrm{De} = 1$, $\beta = 0.5$, $h^* = 0.05$, and $c/R_L = 0.75$. For large values of $D_L l_L^4/D_S l_S^4$, corresponding to relatively short tails, we find that $U_z > 0$. Below a critical value, however, the velocity changes sign once the tail becomes too long and the swimmer propels in the direction of the prolate spheroid. From this figure we estimate that the crossover occurs

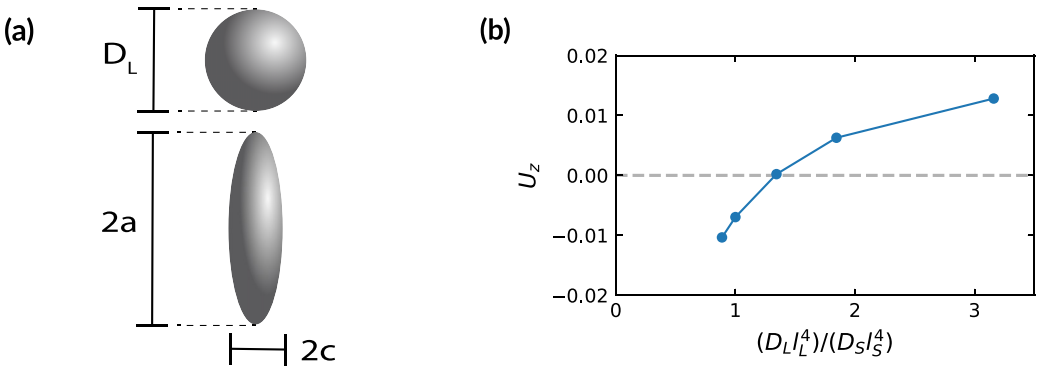

FIG. 9. (a) Schematic of an axisymmetric swimmer with a spherical head and prolate spheroidal tail oriented along the vertical z direction. (b) Swimming velocity U_z as a function of the ratio $D_L l_L^4/D_S l_S^4$ for the case of $c/R_L = 0.75$, De $= 1$, $\beta = 0.5$, and $h^* = 0.05$. From far-field hydrodynamic interactions, we predict that the swimmer shown in (a) should self-propel in the direction of the spherical head if $D_L l_L^4/D_S l_S^4 > 1$. From this set of simulations, we find that U_z changes sign at a value of approximately 1.3; we expect this value to converge to unity as h^* increases and the far-field approximation becomes more accurate.

at approximately 1.3, which is remarkably close to our critical value of unity predicted above. Considering the many far-field assumptions made above, we anticipate that the measured value of $D_L l_L^4/D_S l_S^4$ for which U_z changes sign will converge to unity as h^* is increased.

C. Extension to different swimming gaits and configurations

We conclude our work by illustrating how the simple theory and physical insight we have developed can be easily extended to a variety of microswimmer configurations. For example, consider the situation illustrated in Fig. 10, where the swimmer consists of a large sphere (head) of diameter D_L flanked by two smaller spheres of diameter D_S, each offset from the symmetry axis by an angle equal to α and located a (dimensional) distance h' from the center of the large sphere. This swimmer can undergo torque-free motion by rotating each of the smaller spheres at equal rotation rates directed in opposite directions. We can derive an estimate for the speed of this swimmer in the z direction, by again considering the net thrust on the microswimmer via Eq. (9) as

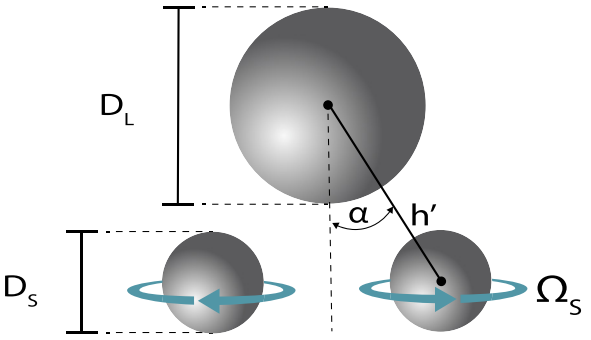

FIG. 10. Illustration of a proposed three-sphere swimmer that translates in a viscoelastic fluid by rotating the two smaller spheres located at its rear.

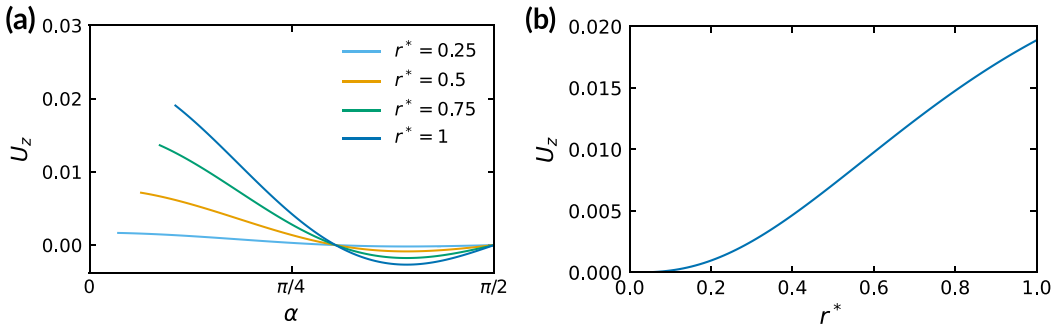

FIG. 11. Velocity U_z of the three-sphere swimmer illustrated in Fig. 10 at De = 1, $\beta = 0.5$, and $h^* = 1$. In (a) the velocity is plotted as a function of the angle α and the size ratio r^* and indicates that the speed of the swimmer $U = |U_z|$ is maximized by selecting the smallest angle and largest size ratio possible. Note that the range of α values considered for each curve is given by $\alpha = \alpha_{\min} = 1/(1 + h^* + r^*)$ to $\alpha = \pi/2$, where $\alpha_{\min}$ is the smallest achievable angle for a given size ratio (i.e., taking into account the finite size of the spheres). In (b) the velocity is plotted as a function of r^*, assuming $\alpha = \alpha_{\min}$.

well as balancing the net drag of $6\pi(1 + 2r^*)$, viz.,

$$U_z = \frac{2\cos\alpha}{1 + 2r^*}\left(1 + \frac{1}{6}\nabla^2\right)u_r^S(\theta = \alpha, r_S = h). \tag{34}$$

Again, splitting U_z into the terms including and not including the Laplacian in Eq. (34), i.e., $U_z = U_z^0 + U_z^{(HO)}$, we obtain the following result for the speed in the z direction of this three-sphere swimmer:

$$U_z^0 = \mathrm{De}(1-\beta)r^{*3}\frac{(1+h^*)^2(1+h^*+3r^*)(\cos\alpha)(1+3\cos 2\alpha)}{2(1+h^*+r^*)^5(1+2r^*)}, \tag{35}$$

$$U_z^{(HO)} = -\mathrm{De}(1-\beta)r^{*3}\frac{[2(1+h^*)^3+6(1+h^*)^2r^*+15(1+h^*)r^{*2}-3r^{*3}](\cos\alpha)(1+3\cos 2\alpha)}{6(1+h^*+r^*)^7(1+2r^*)}. \tag{36}$$

We can simplify this expression significantly by considering a specific gap distance, e.g., $h^* = 1$:

$$U_z = \mathrm{De}(1-\beta)r^{*3}\frac{\{80+3r^*[72+r^*(46+13r^*)]\}(\cos\alpha)(1+3\cos 2\alpha)}{6(2+r^*)^7(1+2r^*)}. \tag{37}$$

We illustrate how the velocity in the z direction depends on the tilt angle α and the size ratio r^* in Fig. 11 [assuming De = 1 and $\beta = 0.5$ since the dependence on these variables is already clear from Eq. (37)]. In Fig. 11(a) we see that velocity of the swimmer shows a complex dependence on α, actually changing sign at an intermediate value of α. The speed $|U_z|$ appears to be maximized by minimizing the tilt angle α and maximizing the size of the smaller spheres, i.e., r^*. Note that this is distinct from the two-sphere swimmer, whose swimming speed vanishes as the size ratio approaches unity. We suspect that the increase in swimming speed with respect to r^* in this case is analogous to the mechanism described for the two-sphere swimmer; i.e., an increase in size of the spinning tail spheres for a fixed rotation rate would lead to more fluid being advected to the rear of the swimmer, thereby creating a net imbalance of pressure on the entire swimmer that acts as a thrust. Note that since the head does not rotate, there is no elastic push back on the tail. Of course, as r^* increases, the minimum achievable angle $\alpha_{\min}$ increases since the two smaller spheres cannot overlap, and it is straightforward to calculate this minimum angle using geometry as $\alpha_{\min} = r^*/(1 + h^* + r^*)$. We plot the velocity of the swimmer assuming $\alpha = \alpha_{\min}$ in Fig. 11(b). This concludes our analysis of the

three-sphere swimmer and illustrates how one can quickly generate predictions for the swimming speed of newly proposed swimmer configurations through the general framework suggested here.

IV. CONCLUSION

In summary, we have examined a simple model swimmer in a viscoelastic fluid that is both force- and torque-free using analytical and numerical calculations in an effort to understand how the interaction between swirling flow and fluid elasticity impacts microorganism motility. The theory and numerical simulations show excellent agreement and predict that the torque-free two-sphere swimmer translates in the direction of the slower-rotating larger sphere. Furthermore, we predict that the swimming speed increases nearly linearly with the Deborah number (measuring the elasticity of the fluid) and $1-\beta$ (i.e., the concentration of polymer in the surrounding fluid). The speed shows a nonmonotonic dependence on the relative size of the two spheres, r^*, with a maximum reached at a value of $r^* \approx 0.75$. By examining the tractions exerted on the surface of the swimmer and the surrounding flow field, we find that the swimmer generates thrust from regions of high pressure surrounding the fast-spinning tail of the swimmer. Upon performing an approximate calculation using literature values for an actual swimming microorganism, i.e., *E. coli*, we find that the speeds predicted are remarkably close to the increase in speed *E. coli* experiences when transitioning from swimming in a Newtonian fluid to a viscoelastic fluid. This suggests that the extra thrust generated from the coupling of rotational to translational motion due to fluid elasticity may be one of the dominant mechanisms in the speed enhancement experienced by bacteria such as *E. coli* in viscoelastic fluids. Finally, we demonstrated how the theory can be quickly extended to different microswimmer configurations and gaits, illustrating its potential utility, for example, in the design of new synthetic swimmers that can be used in future studies on the effect of fluid rheology on motility. We look forward to the verification of our theoretical work via future experiments.

ACKNOWLEDGMENTS

J.P.B. was supported by a National Science Foundation (NSF) Graduate Research Fellowship (Grant No. DGE 1656518). This work was also supported by NSF Grant No. CBET 1803765.

APPENDIX: DERIVATION OF LUBRICATION THEORY

To derive an approximation of the pressure in the thin-gap region between the two spheres of the two-sphere swimmer, we apply the lubrication approximation to the flow in the gap [42]. For this analysis, we operate in a cylindrical coordinate system aligned with the axis of motion and centered between the two spheres. As is often done in lubrication theory, we approximate the distance of the two surfaces from the center of the gap using a Taylor series expansion truncated at the quadratic term, which of course is valid in the limit of $h_{\text{sep}}/R_L \ll 1$ and $h_{\text{sep}}/R_S \ll 1$,

$$h_L = \frac{h_{\text{sep}}}{2} + \frac{1}{2}\frac{r^2}{R_L}, \tag{A1}$$

$$h_S = \frac{h_{\text{sep}}}{2} + \frac{1}{2}\frac{r^2}{R_S}, \tag{A2}$$

where h_L and h_S correspond to the distance from the center of the gap of the surfaces of the larger and the smaller sphere, respectively, and r is the radial coordinate (dimensional) in cylindrical coordinates. After applying the lubrication approximation, conservation of momentum in the θ direction is given by

$$\mu_s \frac{\partial^2 u_\theta}{\partial z^2} + \frac{\partial \tau^p_{\theta z}}{\partial z} = \frac{1}{r}\frac{\partial p}{\partial \theta} = 0. \tag{A3}$$

In the above, $\frac{\partial p}{\partial \theta} = 0$ due to symmetry and all quantities are dimensional (note that this is in contrast to the main text and is done for clarity in presentation). In the radial direction, conservation of momentum is given by

$$\frac{\partial p}{\partial r} = -\frac{\tau^p_{\theta\theta}}{r}. \tag{A4}$$

Because the flow in the gap is simple shear flow to leading order (the flow direction being the azimuthal θ direction), we can write the polymeric shear stress as

$$\tau^p_{\theta z} = \mu_p \frac{\partial u_\theta}{\partial z}. \tag{A5}$$

Combining Eqs. (40) and (42), we find that the velocity in the θ direction is governed by the one-dimensional Laplace equation

$$\frac{\partial^2 u_\theta}{\partial z^2} = 0. \tag{A6}$$

Consequently, the solution must be given by $u_\theta = C_1(r)z + C_2(r)$, where $C_1(r)$ and $C_2(r)$ are arbitrary functions of r. These functions can be easily found by applying the boundary conditions at the surface of the large and the small sphere:

$$u_\theta(z = h_L) = r\Omega_L = C_1 h_L + C_2, \tag{A7}$$

$$u_\theta(z = -h_S) = -r\Omega_S = -C_1 h_S + C_2. \tag{A8}$$

Through some simple algebra, we find that C_1 and C_2 are given by

$$C_1 = \frac{r(\Omega_L + \Omega_S)}{h_S + h_L}, \tag{A9}$$

$$C_2 = C_1 h_S - r\Omega_S. \tag{A10}$$

To derive an expression for the pressure in the gap, we must integrate Eq. (A4) with respect to the radial coordinate. Because the flow is locally simple shear flow, the hoop stress $\tau^p_{\theta\theta}$ is given by [29]

$$\tau^p_{\theta\theta} = 2\lambda\mu_p\left(\frac{\partial u_\theta}{\partial z}\right)^2 = 2\lambda\mu_p C_1^2. \tag{A11}$$

The last equality comes from the fact that $u_\theta = C_1 z + C_2$. With $\tau^p_{\theta\theta}$ now determined, we can integrate Eq. (A4) with respect to r, yielding

$$p = p_\infty - 2\lambda\mu_p \int_\infty^r \frac{C_1^2(\sigma)}{\sigma} d\sigma, \tag{A12}$$

$$p = p_\infty + 2\lambda\mu_p \int_r^\infty \frac{C_1^2(\sigma)}{\sigma} d\sigma, \tag{A13}$$

where σ is a dummy variable for the radial coordinate and $p_\infty = p(r \to \infty)$. Upon substituting our expressions for C_1, h_S, and h_L into the above integral and performing the integration, we obtain

$$p = p_\infty + \lambda\mu_p \frac{(\Omega_S + \Omega_L)^2}{b(h_{\text{sep}} + br^2)}, \tag{A14}$$

where $b = \frac{1}{2}(R_S^{-1} + R_L^{-1})$. If we divide both sides of this expression by $\mu_0\Omega_S$ and make use of our definitions for Ω^*, h^*, r^*, etc. presented in the main text, we arrive at the dimensionless version of this expression, i.e., Eq. (18).

The most significant result from this short lubrication theory is found when we integrate this pressure [i.e., Eq. (A14)] over the surfaces of the large and the small sphere to see if there is a net thrust created by the high pressure in the gap region, that is,

$$F_{\text{thrust}} = F_{\text{pres},L} + F_{\text{pres},S} \tag{A15}$$

$$= 2\pi \int_0^{R_S} (p - p_\infty) r dr - 2\pi \int_0^{R_S} (p - p_\infty) r dr \tag{A16}$$

$$= 0, \tag{A17}$$

where $F_{\text{pres},L}$ and $F_{\text{pres},S}$ are the integrated net forces due to pressure exerted on the large and the small sphere, respectively. Note that we have only integrated over the inner region where lubrication theory is expected to hold. It is clear from this that lubrication theory predicts no net propulsion of the swimmer and that the interaction of the outer region (of size R_S) must be included to describe a nonzero pressure thrust on the swimmer. Therefore, this region provides terms that go to zero like some power of h_{sep}/R_S resulting in the propulsion speed being regular as the gap goes to zero. This justifies our use of Eqs. (12) and (13) in the limit of $h^* \to 0$ in the main text and is supported by the results of Fig. 4.

[1] E. Lauga and T. R. Powers, The hydrodynamics of swimming microorganisms, Rep. Prog. Phys. **72**, 096601 (2009).

[2] J. Elgeti, R. G. Winkler, and G. Gompper, Physics of microswimmers—Single particle motion and collective behavior: A review, Rep. Prog. Phys. **78**, 056601 (2015).

[3] C. Bechinger, R. Di Leonardo, H. Löwen, C. Reichhardt, G. Volpe, and G. Volpe, Active particles in complex and crowded environments, Rev. Mod. Phys. **88**, 045006 (2016).

[4] S. Yazdi and A. M. Ardekani, Bacterial aggregation and biofilm formation in a vortical flow, Biomicrofluidics **6**, 044114 (2012).

[5] A. Houry, M. Gohar, J. Deschamps, E. Tischenko, S. Aymerich, A. Gruss, and R. Briandet, Bacterial swimmers that infiltrate and take over the biofilm matrix, Proc. Natl. Acad. Sci. U.S.A. **109**, 13088 (2012).

[6] D. P. Wolf, L. Blasco, M. A. Khan, and M. Litt, Human cervical mucus. I. Rheologic characteristics, Fertil. Steril. **28**, 41 (1977).

[7] J. P. Celli, B. S. Turner, N. H. Afdhal, S. Keates, I. Ghiran, C. P. Kelly, R. H. Ewoldt, G. H. McKinley, P. So, S. Erramilli *et al.*, *Helicobacter pylori* moves through mucus by reducing mucin viscoelasticity, Proc. Natl. Acad. Sci. U.S.A. **106**, 14321 (2009).

[8] *Complex Fluids in Biological Systems: Experiment, Theory, and Computation*, edited by S. E. Spagnolie (Springer, New York, 2015).

[9] E. M. Purcell, Life at low Reynolds number, Am. J. Phys. **45**, 3 (1977).

[10] D. Patra, S. Sengupta, W. Duan, H. Zhang, R. Pavlick, and A. Sen, Intelligent, self-powered, drug delivery systems, Nanoscale **5**, 1273 (2013).

[11] W. Gao and J. Wang, Synthetic micro/nanomotors in drug delivery, Nanoscale **6**, 10486 (2014).

[12] O. S. Pak, L. Zhu, L. Brandt, and E. Lauga, Micropropulsion and microrheology in complex fluids via symmetry breaking, Phys. Fluids **24**, 103102 (2012).

[13] T. Qiu, T.-C. Lee, A. G. Mark, K. I. Morozov, R. Münster, O. Mierka, S. Turek, A. M. Leshansky, and P. Fischer, Swimming by reciprocal motion at low Reynolds number, Nat. Commun. **5**, 5119 (2014).

[14] N. C. Keim, M. Garcia, and P. E. Arratia, Fluid elasticity can enable propulsion at low Reynolds number, Phys. Fluids **24**, 081703 (2012).

[15] C. Datt, B. Nasouri, and G. J. Elfring, Two-sphere swimmers in viscoelastic fluids, Phys. Rev. Fluids **3**, 123301 (2018).

[16] L. W. Rogowski, H. Kim, X. Zhang, and M. J. Kim, *Proceedings of the 15th International Conference on Ubiquitous Robots, Honolulu, 2018* (IEEE, Piscataway, 2018), pp. 5–10.

[17] L. Rogowski, J. Ali, X. Zhang, H. Fu, and M. J. Kim, Propulsion of microparticles in nonlinearly viscoelastic fluids through symmetry breaking, in *73rd Annual Meeting of the APS Division of Fluid Dynamics* (Bulletin of the American Physical Society, 2020), abstract: U04.00004.
[18] J. A. Puente-Velázquez, F. A. Godínez, E. Lauga, and R. Zenit, Viscoelastic propulsion of a rotating dumbbell, Microfluid. Nanofluid. **23**, 108 (2019).
[19] H. C. Berg, *E. coli in Motion* (Springer Science + Business Media, New York, 2008).
[20] E. Lauga, Bacterial hydrodynamics, Annu. Rev. Fluid Mech. **48**, 105 (2016).
[21] A. Castillo, W. L. Murch, J. Einarsson, B. Mena, E. S. G. Shaqfeh, and R. Zenit, Drag coefficient for a sedimenting and rotating sphere in a viscoelastic fluid, Phys. Rev. Fluids **4**, 063302 (2019).
[22] J. P. Binagia, A. Phoa, K. D. Housiadas, and E. S. G. Shaqfeh, Swimming with swirl in a viscoelastic fluid, J. Fluid Mech. **900**, A4 (2020).
[23] K. D. Housiadas, J. P. Binagia, and E. S. Shaqfeh, Squirmers with swirl at low Weissenberg number, J. Fluid Mech. **911**, A16 (2021).
[24] B. Liu, T. R. Powers, and K. S. Breuer, Force-free swimming of a model helical flagellum in viscoelastic fluids, Proc. Natl. Acad. Sci. U.S.A. **108**, 19516 (2011).
[25] S. E. Spagnolie, B. Liu, and T. R. Powers, Locomotion of Helical Bodies in Viscoelastic Fluids: Enhanced Swimming at Large Helical Amplitudes, Phys. Rev. Lett. **111**, 068101 (2013).
[26] V. Angeles, F. Godinez, J. Puente-Velazquez, R. Mendez, E. Lauga, and R. Zenit, Front-back asymmetry controls the impact of viscoelasticity on helical swimming, Phys. Rev. Fluids **6**, 043102 (2021).
[27] J. G. Oldroyd, On the formulation of rheological equations of state, Proc. R. Soc. London Ser. A **200**, 523 (1950).
[28] G. J. Elfring and E. Lauga, in *Complex Fluids in Biological Systems*, edited by S. Spagnolie (Springer, New York, 2015), pp. 283–317.
[29] R. B. Bird, R. C. Armstrong, and O. Hassager, *Dynamics of Polymeric Liquids*, 2nd ed. (Wiley, New York, 1987), Vol. 1.
[30] S. Kim and S. J. Karrila, *Microhydrodynamics: Principles and Selected Applications* (Courier, Chelmsford, 2013).
[31] F. Ham, K. Mattsson, and G. Iaccarino, *Center for Turbulence Research Annual Research Briefs* (Stanford University, Stanford, 2006), pp. 243–261.
[32] D. Richter, G. Iaccarino, and E. S. Shaqfeh, Simulations of three-dimensional viscoelastic flows past a circular cylinder at moderate Reynolds numbers, J. Fluid Mech. **651**, 415 (2010).
[33] S. Padhy, E. S. G. Shaqfeh, G. Iaccarino, J. F. Morris, and N. Tonmukayakul, Simulations of a sphere sedimenting in a viscoelastic fluid with cross shear flow, J. Non-Newtonian Fluid Mech. **197**, 48 (2013).
[34] M. Yang, S. Krishnan, and E. S. G. Shaqfeh, Numerical simulations of the rheology of suspensions of rigid spheres at low volume fraction in a viscoelastic fluid under shear, J. Non-Newtonian Fluid Mech. **233**, 181 (2016).
[35] A. Saadat, C. J. Guido, G. Iaccarino, and E. S. G. Shaqfeh, Immersed-finite-element method for deformable particle suspensions in viscous and viscoelastic media, Phys. Rev. E **98**, 063316 (2018).
[36] J. P. Binagia, C. J. Guido, and E. S. Shaqfeh, Three-dimensional simulations of undulatory and amoeboid swimmers in viscoelastic fluids, Soft Matter **15**, 4836 (2019).
[37] R. Fattal and R. Kupferman, Constitutive laws for the matrix-logarithm of the conformation tensor, J. Non-Newtonian Fluid Mech. **123**, 281 (2004).
[38] M. A. Hulsen, R. Fattal, and R. Kupferman, Flow of viscoelastic fluids past a cylinder at high Weissenberg number: Stabilized simulations using matrix logarithms, J. Non-Newtonian Fluid Mech. **127**, 27 (2005).
[39] C. G. Broyden, A class of methods for solving nonlinear simultaneous equations, Math. Comput. **19**, 577 (1965).
[40] A. Patteson, A. Gopinath, M. Goulian, and P. Arratia, Running and tumbling with *E. coli* in polymeric solutions, Sci. Rep. **5**, 15761 (2015).
[41] H. Giesekus, A simple constitutive equation for polymer fluids based on the concept of deformation-dependent tensorial mobility, J. Non-Newtonian Fluid Mech. **11**, 69 (1982).
[42] L. G. Leal, *Advanced Transport Phenomena: Fluid Mechanics and Convective Transport Processes* (Cambridge University Press, Cambridge, 2007), Vol. 7.